Determination of the Optimum Filter Function for SPECT Imaging

David R. Gilland, Benjamin M. W. Tsui, William H. McCartney, J. Randolph Perry, and Jan Berg

Department of Radiology and Curriculum in Biomedical Engineering, The University of North Carolina at Chapel Hill; and General Electric Company, Medical Systems Group, Milwaukee, Wisconsin

An observer study was performed in order to evaluate several filters used in SPECT imaging. The filters were applied to the simulated projection data of a uniform activity density cylinder which contained a cold, spherical lesion, 2 cm in diameter. The data incorporated the effects of the detector and scatter response functions, photon attenuation, and noise. Reconstructed transaxial images were used in 2AFC and ROC observer studies testing lesion detectability. In the 2AFC experiment, the Hanning filter scored lowest and did not show a optimum cutoff frequency. The Butterworth filter performed better and showed a well-defined optimum cutoff frequency at 0.15 cycles/pixel. The Metz filter performed as well as the optimum Butterworth but did not show an optimum power factor. In the ROC study, a high power Metz filter demonstrated an ROC curve of lower A_z index and different shape from a lower power Metz filter and the optimum Butterworth filter.

T he problem of noise in single photon emission computed tomography (SPECT) is usually handled with the application of low-pass, digital filters designed to suppress high spatial frequencies where no signal is present or where noise dominates the signal. Most SPECT filter functions allow the user to control the degree of high frequency suppression by choosing a cutoff frequency, or similar filter parameter, which determines where the filter rolls off to zero gain. The location of this cutoff frequency determines how the filter will affect both image noise and resolution. Low cutoff frequencies provide good noise suppression, but they can blur the image. Higher cutoff frequencies can preserve resolution, but often suppress noise insufficiently. There should exist an optimum cutoff frequency for a particular filter function which compromises the trade-off between noise suppression and spatial resolution degradation. This optimum will depend on factors such as the detector response function, the spatial frequencies of the object, and the count density of the image. The purpose of this study was to determine the optimum filter function and cutoff frequency for simulated SPECT images of a simple phantom.

The criterion which we have used in judging the performance of a filter function is in terms of its effect on lesion detectability. We have performed observer performance studies using computer simulated images in order to quantify lesion detectability and to determine the optimum parameters for three filter types. Subjects are shown images on a video monitor and are rated on their ability to detect a lesion.

In order to make the simulated images resemble acquired clinical images as closely as possible, we have modeled and incorporated into the simulation many of the physical phenomena of an actual clinical liver study. The simulation incorporates the effects of photon attenuation, and the detector and scatter response functions. Also, noise levels are similar to those found in clinical liver studies.

The results of this study can have important clinical applications. SPECT filters can greatly affect the quality of clinical images by their degree of smoothing. Determining the best filter and the proper degree of smoothing can help to ensure the most accurate diagnosis. These results can also help speed image processing time since a proper filter function is often chosen clinically by the tedious and time-consuming process of trial and error.

BACKGROUND

Filter Operation

The filtering of SPECT images has been performed at three different stages of the reconstruction algorithm. Originally, the smoothing filter was combined with the ramp filter which was applied one-dimensionally in the transverse direction of the projection data. However, when sagittal, coronal, or oblique images are reconstructed from multiple slice, transaxial data which has been smoothed in this way, streaking can occur in a direction parallel to the transaxial plane. These streaks are the result of preferential smoothing in the transaxial direction.

In order to overcome this problem, algorithms have been developed which perform separate smoothing in the axial and transaxial directions. A one-dimensional smoothing filter is applied first in the axial direction of the projection data and then in the transaxial direction along with the ramp filter during the reconstruction. While this technique of separable smoothing in the axial and transaxial directions can eliminate streaking, it has been shown that it does not result in a three-dimensional isotropic point response (1). Therefore, this technique is unsuitable for oblique tomography.

The solution to this problem has come about with the application of a two-dimensional, radially symmetric smoothing function to the projection data before reconstruction. When this filter is combined with the ramp in the transaxial direction, the resultant point response is isotropic (1). Therefore, this algorithm is well-suited for the sagittal, coronal, and oblique reconstructions. In addition, this algorithm is superior in noise handling to the algorithms previously discussed (1).

SPECT Filters

There are basically two types of filters that are used in SPECT imaging; the smoothing and enhancement filters. The smoothing filters are low-pass filters and allow the user to select the cutoff frequency which determines the location of the filter rolloff. An example of this filter type is the Hanning filter. The Hanning filter is defined in the frequency domain as,

$$H(\nu) = 0.5 + 0.5 \cos(\pi\nu/\nu_c) \qquad 0 \le |\nu| \le \nu_c. \tag{1}$$
$$= 0 \qquad \text{otherwise.}$$

The cutoff frequency, ν_c, determines when the function reaches zero gain. The frequency response of the Hanning filter is illustrated in Figure 1A.

The Butterworth filter is another example of a smoothing filter and it is defined in the frequency domain as,

$$B(\nu) = \frac{1}{\left[1 + \left(\dfrac{\nu}{\nu_c}\right)^n\right]^{\frac{1}{2}}}. \tag{2}$$

In contrast to the Hanning, the Butterworth filter cutoff frequency is defined as the point where the gain is down to 0.707. The shape of the Butterworth differs from the Hanning in that this filter maintains a value close to one at low frequencies and has a steeper rolloff. The parameter n determines the steepness of the rolloff. The frequency response of the Butterworth is illustrated in Figure 1B.

Another class of filters which have been used in SPECT imaging is the enhancement and restoration filters (2-4). These filters attempt to recover the resolution lost in the detection process by exceeding unity gain over a desired frequency band. Because of the domination of noise at high frequencies, enhancement filters at some point must also rolloff to zero gain. An example of a enhancement filter is the Metz filter. This filter is defined in the frequency domain as,

$$M(\nu) = \frac{1 - [1 - \text{MTF}^2(\nu)]^X}{\text{MTF}(\nu)}. \tag{3}$$
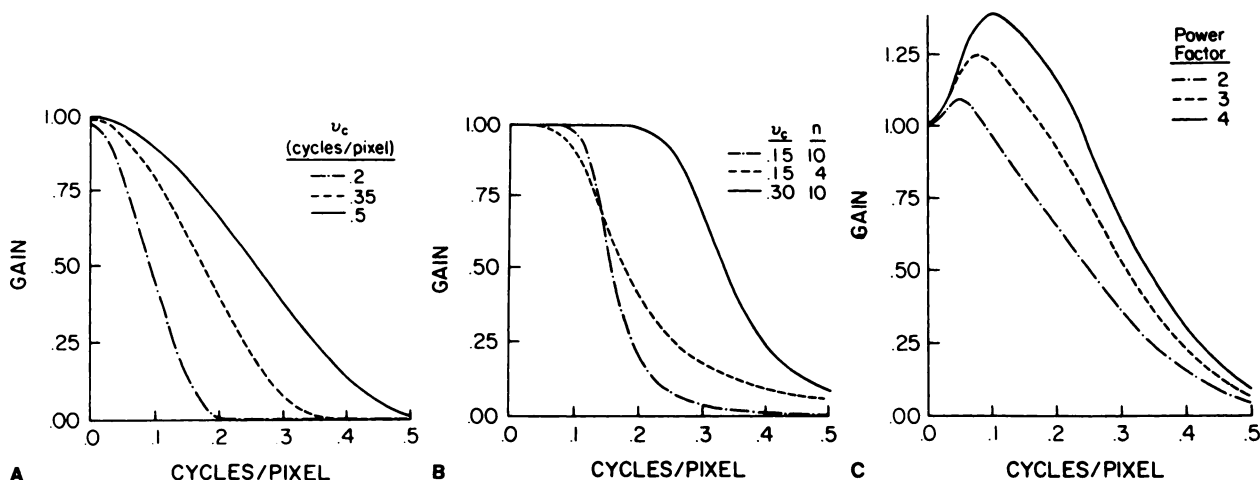
The Metz filter is a combination of deconvolution and

FIGURE 1

A: Frequency response of Hanning Filter. The plots show the Hanning Filter at three cutoff frequencies (ν_c). The cutoff frequency is the point at which the filter reaches zero gain. B: Frequency response of Butterworth Filter. The plots show the Butterworth Filter at two cutoff frequencies (ν_c) and two power factors (n). The cutoff frequency is the point at which the gain is down to 0.707. The power factor controls the steepness of the rolloff. C: Frequency response of Metz Filter. The plots show the Metz filter at three power factors. The power factor determines when the filter changes from the inverse MTF to a rolloff to zero gain. The MTF was calculated based on a source located 25 cm from the collimator face and at a depth of 12.5 cm into the scattering medium.

smoothing filters. The parameter X determines the extent to which the filter follows the inverse MTF before rolling-off to zero gain. The frequency response of the Metz filter is illustrated in Figure 1C.

It has been reported previously that visually more pleasing images have resulted when a generalized exponential of the form,

$$H(\nu) = \exp(-\nu^P/S), \quad (4)$$

is used in place of the MTF in the Metz filter (2). The parameters P and S can be adjusted according the count density and power spectrum of the image. This form of the Metz filter also produced images with a lower mean-squared-error than the MTF form.

METHODS

Image Simulation

The test images for the observer study were reconstructed from simulated projection images. The simulation incorporated effects of the detector response as well as image noise and involved the following process: (1) determine the three-dimensional activity distribution of the object, (2) solve analytically for the projection images over all view angles considering photon attenuation, (3) digitize the simulated projection data, (4) smooth the data with an estimation of the detector response function including scatter, (5) add count-dependent Poisson noise to these projections, (6) apply the test filter, (7) reconstruct the transaxial images.

The simulated object consisted of a cylindrical body, 25 cm in diameter, 40 cm in height, with a uniform distribution of radioactivity. Embedded within the cylinder was a spherical lesion, 2 cm in diameter and void of radioactivity. A cold tumor of this size was simulated in order to model a clinical liver study. The location of the tumor was varied randomly.

The attenuated projections of a cold sphere in a hot cylinder were simulated by subtracting the attenuated projections of a hot sphere in a cold cylinder from the attenuated projections of a hot cylinder. Both the subtrahend and minuend projection datasets were calculated for 64 views over 360°, digitized into 64 × 64 matrices, and smoothed with an estimation of the detector response function prior to subtraction. The reason for smoothing these datasets rather than the difference dataset will become apparent at the end of the following discussion on the estimation of the detector response function.

Detector Response Function

The total detector response function consists of the penetration, scatter, and geometric components. With low-energy gamma ray photons, such as ^{99m}Tc, and a properly designed collimator, the penetration component is negligible and was disregarded in this simulation. The scatter and geometric components can be considered to act in parallel and are summed in the following way to yield the total detector response function in the frequency domain (5),

$$DRF_T(\nu) = \frac{DRF_G(\nu) + f_s DRF_S(\nu)}{1 + f_s}, \quad (4)$$

where $DRF_T(\nu)$ is the total detector response function, $DRF_G(\nu)$ is the geometric component, $DRF_S(\nu)$ is the scatter component, and f_s is the scatter fraction. The scatter fraction

represents the ratio of scattered to unscattered photons detected and is a function of the depth of the source in the scattering medium. Monte Carlo studies (6) have demonstrated that the scatter and the geometric components are related by a multiplicative function,

$$DRF_s(\nu) = K(\nu) * DRF_G(\nu), \quad (5)$$

where $K(\nu)$ is a function of the scattering conditions, i.e., energy window settings, detector energy resolution, source primary energy, and depth of source in the scattering medium.

An alternate representation of the detector response is the use of the series-equivalent scatter response function (7) where the total response function is:

$$DRF_T(\nu) = DRF_G(\nu) * DRF_S^{series}(\nu). \quad (6)$$

Monte Carlo studies (6) and experimental data (8) have shown that $DRF_S^{series}(\nu)$ is essentially independent of collimation and is a function of only the scattering conditions. Eqs. (4)–(6) can be used to solve for $DRF_S^{series}(\nu)$ in terms of $K(\nu)$ and f_s:

$$DRF_S^{series}(\nu) = \frac{f_s K(\nu) + 1}{1 + f_s}. \quad (7)$$

We chose to use the series-equivalent formulation to approximate the total detector response function because of its simplicity and generality. Given the scattering conditions, $DRF_S^{series}(\nu)$ allows one to determine the total response function for any collimator if the geometric component is known. Based on Monte Carlo data (6) and Eq. (7), we have estimated $DRF_S^{series}(\nu)$ for our experimental situation assuming 140 keV primary energy, 125 keV baseline energy, and 11% detector energy resolution. The function $K(\nu)$ was determined by fitting the Monte Carlo data with a two Gaussian approximation,

$$K(\nu) = a \cdot \exp[-\nu^2/2s_1^2] \\ + (1 - a) \cdot \exp[-\nu^2/2s_2^2], \quad (8)$$

where a, s_1, and s_2 are functions of the source energy, the energy window, and the source depth. For our estimation, a was close to one, and we disregarded the second Gaussian. The scatter fraction, f_s, was dependent upon the source depth, d, in the following way,

$$f_s = 0.07d, \quad (9)$$

where d is in units of cm.

The geometric component of the detector response is a function of the collimator and the distance of the object from the collimator face. For this study $DRF_G(\nu)$ was estimated from line spread function measurements in air at different distances from a General Electric collimator. We approximated the line spread function with a Gaussian function and found that over realistic collimator-object distances, σ of the Gaussian is linearly related to the distance from the collimator face, D,

$$\sigma = 0.02446D + 0.1793, \quad (10)$$

where D is in units of cm. The Fourier transform of this Gaussian function is an estimation of geometric response function, $DRF_G(\nu)$, and this was then multiplied by $DRF_S^{series}(\nu)$ to get the total response function in the frequency domain.

Thus for a given source energy, energy window, and detector energy resolution, the total detector response function is

dependent upon (1) the distance of the source from the detector and (2) the depth of the source in the scattering medium. The problem with simulating the detector response in projection images is that the source is distributed over a range of distances from the detector as well as over a range of depths in the scattering medium. No single detector response function, therefore, precisely describes the blurring in a projection image. To compound the problem, the blurring changes from projection image to projection image since the distance of the source to the detector and the depth of the source in the scattering medium change with angle.

In order to partially model the distance dependence of the detector response in this simulation, we smoothed with the detector response function the subtrahend and minuend datasets rather than the difference dataset. This allowed us to simulate the differential blurring of the lesion with projection angle. In the attenuated projection dataset of the hot lesion in the cold cylinder, we calculated a detector response function for each angle based on the distance of the lesion to the detector and the depth of the lesion in the scattering medium. The attenuated projection dataset of the hot cylinder was smoothed over all angles with an "average" detector response in which the distance to the detector equaled the radius of rotation (25 cm) and the depth of the source in the scattering medium equaled the cylinder radius (12.5 cm). The data sets were then subtracted as described earlier, resulting in the incorporation of attenuation and the detector response in the

FIGURE 2
Simulated projection image of object distribution without noise. The simulation incorporates the detector response function including scatter. The lesion is located near the center of the image. B: Simulated projection image with added Poisson noise. The average count density near the center of the projection image is 150 counts/pixel. C: Filtered projection image. The image in Figure 2B has been filtered with the Butterworth Filter (ν_c = 0.15, n = 10). D: Reconstructed image. The projection dataset from Figure 2C with 64 views has been reconstructed at the level of the lesion center. The reconstructed images were used in the observer study.

simulated projections of a cold sphere in a hot cylinder. An example of such a projection image is shown in Figure 2A.

Image Noise

The next step in the image simulation was to add noise to the projection data using a Poisson random number generator. The variance of each pixel in the resulting projection image was equal to the expected, or noise-free, pixel value. The noise level was chosen so that the processed, reconstructed image would score ~75% correct in a two-alternative-forced-choice (2AFC) preliminary observer study. This resulted in projection images with ~150 counts per pixel. This noise level is typical of a clinical liver study. An example of a projection image with added noise is shown in Figure 2B.

Filter Functions

The filter functions evaluated in this study included the Hanning (cutoff frequencies 0.2, 0.25, 0.3, 0.35, 0.4, 0.45 cycles/pixel), Butterworth (cutoff frequencies 0.1, 0.125, 0.15, 0.175, 0.2, 0.225 cycles/pixel), and Metz (power factors 2, 4, 6, 8, 10, 12) filters. Within each filter type, the cutoff frequencies or power factors were chosen as those which, from a subjective standpoint, bracketed the optimum. The power term in the Butterworth filter function was held fixed at 10. This value was chosen because the resulting Butterworth filter has a flatter response than the Hanning filter at low frequencies but does not rolloff so sharply as to produce ringing artifacts. We were interested in the effects of this flat, low-frequency response on lesion detectability. The form of the Metz filter tested in this study was the MTF form described earlier. The MTF used in the filter included scatter and was equivalent to the "average" detector response function used to blur the projections of the cylindrical body.

The filters were applied as two-dimensional, radially symmetric, preprocessing filters. The filtering was performed in the frequency domain by an array processor (Analogic AP400 array processor). A noise projection image processed with a Butterworth filter with a cutoff frequency of 0.15 cycles/pixel and n = 10 is shown in Figure 2C.

Image Reconstruction

The final step of the image simulation was to reconstruct transaxial slices from the filtered projection data. The filtered backprojection technique was used. Before backprojecting, the projection array was linearly interpolated to increase the number of projection values eight times. This projection array was then backprojected into the reconstruction matrix in a nearest neighbor manner. An example of a processed, reconstructed image is shown in Figure 2D.

Observer Study

The observer study was performed using the two-alternative-forced-choice (2AFC) and ROC (9,10) methods. Five biomedical engineers and two radiologists took part in the 2AFC study. In this study, a total of 64 images with lesion and 64 images without lesion were simulated, and those images were processed with each of the filter functions. A trial consisted of 64 image pairs processed with the same filter. The pairing of images with and without lesion was randomized before each trial. Each observer viewed the 64 image pairs processed with each of the filter functions. In addition, the observers viewed the 64 pairs with no smoothing. The images with lesion were reconstructed at the level of the lesion center.
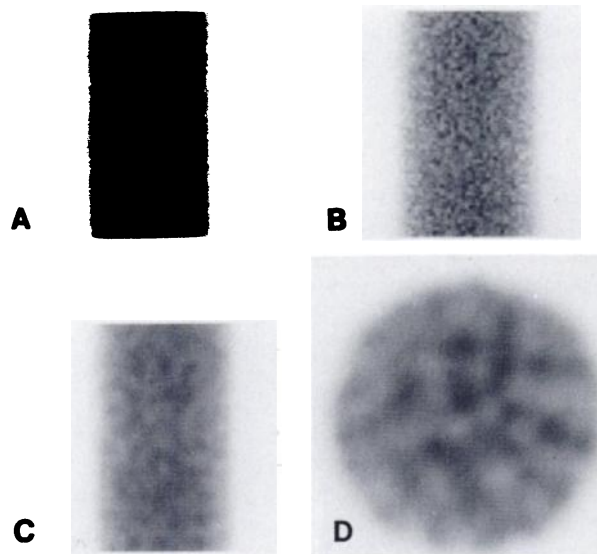
Prior to data collection, the observers were put through a training session in which the actual lesion location was shown to the observer after each response.

Five biomedical engineers took part in the ROC study including three who participated in the 2AFC study. One hundred and eight of the 128 images used in the 2AFC study were used in the ROC study. The remaining 20 images were used for ROC training purposes. Fifty percent of the 108 images contained a lesion. Each observer viewed the 108 images processed with each filter function as well as the 108 images unprocessed. Observers rated on a scale of one to five their confidence in the presence of a lesion. As in the 2AFC study, observers were put through a training session before each trial in which the actual lesion location was shown after each response. The observers were told prior to the study that ~50% of the images contain a lesion.

The display system consisted of an 8-in. black and white monitor with 256 gray levels. The images were normalized such that the mean pixel value was constant across all images. The display map was linear. Pixels 3 s.d. or more above the mean pixel value received full display intensity, and pixels 3 s.d. or more below the mean received the minimum display intensity. Observers were encouraged to view the images at a comfortable distance and to take as long as they liked in making a decision. Most decisions were made within 10 sec.

RESULTS AND DISCUSSION

2AFC Experiment

The results of the 2AFC experiment for the Hanning, Butterworth, and Metz filters are shown in Figures 3A, 3B, and 3C, respectively. The percentage of correct responses has been plotted against cutoff frequency for each filter (against power factor for Metz). The data points represent the weighted mean and standard deviation of the mean for the seven observers. Recall that the cutoff frequency is defined differently for the Hanning and Butterworth filters and that the power factor for the Metz filter determines the degree of enhancement. The control (no filter) is equivalent to an infinite cutoff frequency for the Hanning and Butterworth fil-

ters and has been plotted as such in Figures 3A and 3B. These two curves can be expected to slope down and approach the no-filter data point as the cutoff frequency is increased beyond the range of this study. In Figure 3C, the results of the control image set have been stated explicitly.

A qualitative examination of Figure 3 reveals clearly that smoothing improves lesion detectability in these images. All of the filters tested scored substantially better than the control which received no smoothing. The Hanning filter did not exhibit an optimum cutoff frequency, nor did the Metz filter show an optimum power factor. The Butterworth filter, however, did show a well-defined optimum cutoff frequency near 0.15 cycles/pixel.

The statistical significance of the differences between the 2AFC results was tested using the two-tailed t-test for paired data. We were interested in pairing the Butterworth filter which scored the highest ($\nu_c = 0.15$ cycles/pixel) against other cutoff frequencies for the Butterworth filter, the best Hanning filter ($\nu_c = 0.35$ cycles/pixel), the Metz filter at power 4, and the control. The two-tailed p values from these paired t-tests are shown in the upper portion of Table 1. We also paired the Metz filter at a power of 4 against other Metz filters, the best Hanning filter, and the control. These two-tailed p values are shown in the lower portion of Table 1.

The results in Table 1 can be summarized as follows. The Butterworth ($v_c = 0.15$) and Metz at power 4 scored significantly better than the control at low p levels. The differences among filters, however, are less substantial. The Butterworth filter at the 0.15 cutoff frequency was significantly better than other Butterworth cutoff frequencies tested, except 0.125, at a p level of 0.14. The 0.15 Butterworth filter was not significantly different from the Metz filter at power 4, but both of these filters were better than the best Hanning filter at a p level of 0.14. The Metz filter at a power of 4 was not significantly different from powers 2, 6, or 12.
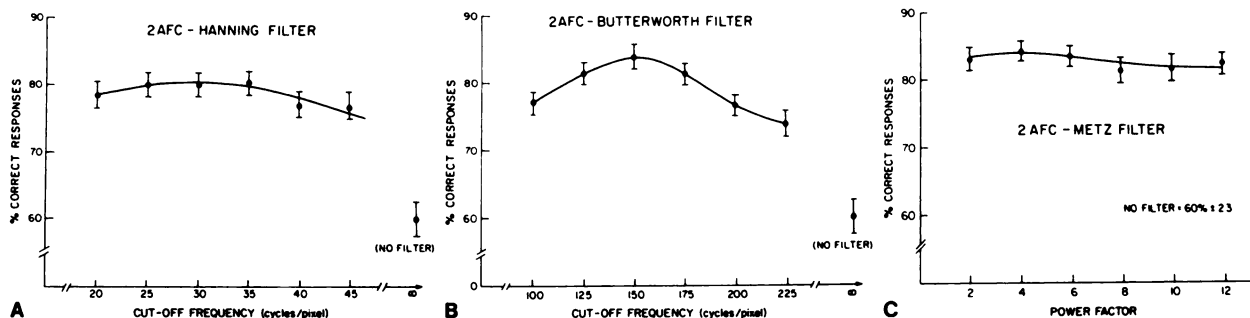

FIGURE 3
A: Results from 2AFC experiment using the Hanning filter. The results do not demonstrate an optimum cutoff frequency. B: Results from 2AFC experiment using the Butterworth Filter. The maximum percent correct occurs at a cutoff near 0.15 cycles/pixel. C: Results from 2AFC experiment using the Metz filter. The results with the Metz filter do not demonstrate an optimum power factor. The scores are approximately equal to the score obtained from the optimum cutoff frequency for the Butterworth filter.

TABLE 1
Two-Tailed p Values from Paired t-Tests
of the Difference in 2AFC Scores

	Butterworth ($\nu_c = 0.15$)
Butterworth ($\nu_c = 0.1$)	0.11
Butterworth ($\nu_c = 0.125$)	0.40
Butterworth ($\nu_c = 0.175$)	0.14
Butterworth ($\nu_c = 0.2$)	0.01
Hanning ($\nu_c = 0.35$)	0.08
Metz (power = 4)	0.46
No filter	0.00

	Metz (power = 4)
Metz (power = 2)	0.90
Metz (power = 6)	0.78
Metz (power = 12)	0.31
Hanning ($\nu_c = 0.35$)	0.14
No filter	0.00

Caution should be exercised in generalizing these results beyond the context of this study. We have tested these filters in terms of lesion detectability in images containing a uniform background. In situations involving structurally more complex images and different diagnostic tasks (such as discrimination) different results are likely. Nevertheless, we feel the results of this study offer important insights into the behavior of these filters in SPECT imaging. It should also be emphasized that the form of the Metz filter used in this study was the MTF form. As reported earlier, King et al. (2) have found the generalized exponential form of the Metz filter produces images substantially more pleasing visually. It will be interesting to test this form in similar observer studies.

A curious finding from this study is the lack of a clearly defined optimum cutoff frequency for the Hanning filter. The relative insensitivity of lesion detectability to changes in cutoff frequency for the Hanning filter may be due in part to the diagnostic task and tumor model employed in this study. Detectability of a simple target in a uniform background may benefit as much from noise suppression as from high spatial resolution, and for this reason, smooth Hanning filters can perform as well as high cutoff frequency Hanning filters which preserve resolution but allow the appearance of high frequency noise.

Unlike the Hanning filter, the Butterworth did demonstrate an optimum cutoff frequency (near 0.15 cycles/pixel). Why the Butterworth demonstrated an optimum cutoff frequency and the Hanning did not is not clear. Insight into why the 0.15 cutoff frequency produced the greatest lesion detectability for the Butterworth filter can be gained by examining the relationship between the filter function cutoff frequency and the size of the detected lesion. Figures 4A, 4B, and 4C, are plots of the Butterworth filter in the spatial domain at cutoff frequencies of 0.125, 0.15, 0.175 cycles/pixel, respectively. Also plotted in each figure is a profile through the lesion center in a projection image in which the lesion is at a distance from the detector approximately equal to the radius of rotation. These figures illustrate the fact that the optimum Butterworth filter cutoff frequency, 0.15 cycles/pixel, is the filter function which is closest in size to the detected lesion. Whether or not this finding can be generalized to lesions of different sizes remains to be tested. If so, it may be possible to use a priori knowledge of lesion size as a guideline for selecting the Butterworth filter cutoff frequency.
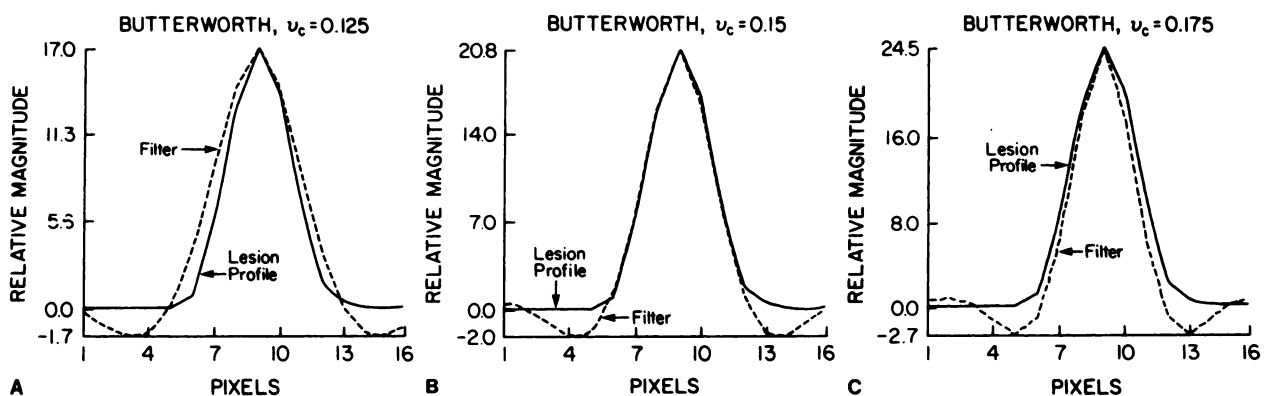

FIGURE 4

A: The two plots are of the Butterworth filter in the spatial domain at a 0.125 cycles/pixel cutoff frequency with n = 10 and a profile through the lesion center from a projection image in which the lesion is at a distance from the detector approximately equal to the radius of rotation. The plots show that the filter is slightly wider than the detected lesion. B: This figure is similar to Figure 4A except at a 0.15 cycles/pixel cutoff frequency. This illustrates that this filter is very close in size to the detected lesion. C: This figure is similar to Figure 4A except at a 0.175 cycles/pixel cutoff frequency. This filter is slightly narrower than the detected lesion.

The data from this 2AFC study suggest that the Hanning is the weakest of the three filter types tested. This is perhaps due to the response of the Hanning filter at low frequencies. Unlike the Butterworth filter which maintains a gain close to one at low frequencies, or the Metz filter which exceeds unit gain in the low frequency range, the Hanning filter drops below unit gain relatively quickly (Fig. 1). Because the signal in nuclear medicine is mainly contained at these low frequencies, this drop-off may be responsible for the decreased detectability with the Hanning filter in this study. Figure 5 shows that contrast of low frequency components in the Hanning filtered image is reduced relative to the Butterworth and Metz images.

The question now is, which of the Butterworth and Metz filters is the optimum filter for this study? The Metz filter at power factors 2, 4, and 6 scored essentially the same as the optimum Butterworth filter. If it is true that the optimum cutoff frequency for the Butterworth filter is dependent upon the lesion size, then the preference should be for the Metz filter since typically one does not know the lesion size a priori. Although their 2AFC scores were similar, Figure 5 shows that the Metz filtered image is qualitatively different than the Butterworth filtered image in that the contrast of low frequency structures is enhanced with the Metz filter. In order to understand better the behavior of the Butterworth and Metz filters and to reveal possible differences between them, we performed an ROC confidence-rating experiment testing the optimum Butterworth filter (cutoff frequency of 0.15 cycles/pixel), the Metz filter

which scored the best (power factor of 4), the Metz filter at power factor 12, and the control.

ROC Results

Figure 6 shows the ROC curves for the Butterworth filter, the Metz filters, and the control. The curves were obtained by fitting each individual observer's confidence-rating data to a binormal ROC curve (11) and then averaging the ROC parameters across observers. Also included in the figure is A_z, or the area under the ROC curve, for each filter. These values were also obtained by averaging each individual observer's A_z score.

The results of testing the statistical significance of the differences between the ROC curves are now presented. As in the 2AFC study, the no-filter ROC data demonstrated a highly significant decrease in observer performance by both bivariate and area tests for all individual observers (12). However, these same tests did not reveal a significant difference between the ROC data of any two filters tested for a majority of the observers. In order to obtain a measure of the significance of differences which combined the results of multiple observers, we performed two-tailed, paired t-tests on the difference in area under the ROC curve, A_z, and on the difference in true positive fraction (TPF) at given false-positive fractions (FPF). In terms of A_z score, there was no significant difference between the Butterworth and Metz at power 4; however, both of these filters performed significantly better than Metz at
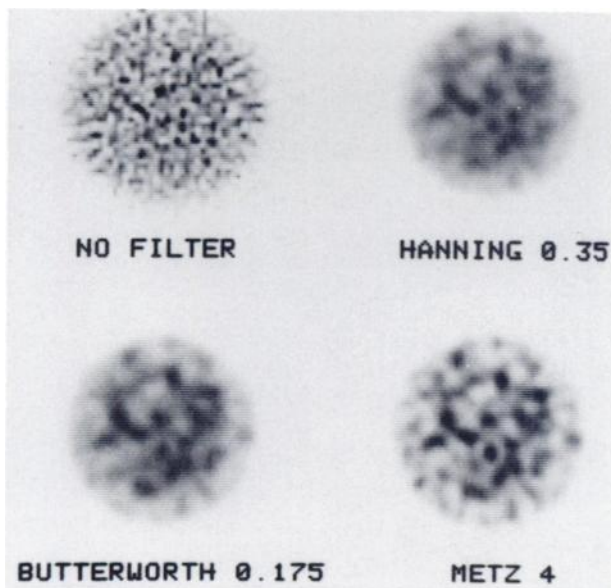
NO FILTER   HANNING 0.35

BUTTERWORTH 0.175   METZ 4

FIGURE 5
Effects of three filters on the reconstructed image. The three filters rolloff at approximately the same frequency range although the shape of each is different (Figures 1A, 1B, and 1C). Each filter affects the image quality differently.
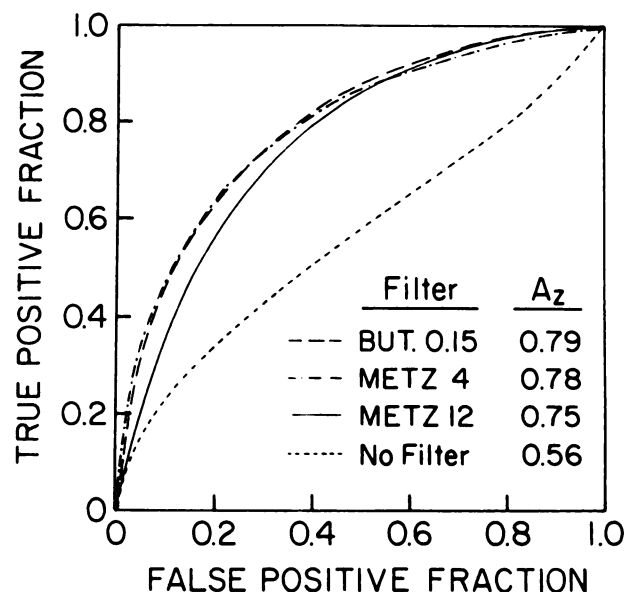
FALSE POSITIVE FRACTION

Filter	A_z
BUT. 0.15	0.79
METZ 4	0.78
METZ 12	0.75
No Filter	0.56

FIGURE 6
ROC curves of three filter functions and the control. The no-filter ROC curve is substantially depressed relative to the filter functions curves. The curves for the Butterworth (v_c = 0.15 cycles/pixel) and the Metz at power 4 were not different, but both were greater than Metz at power 12 at low FPF values.

TABLE 2
Two-Tailed p Values from Paired t-Tests
of the Difference in A_z

	Metz (power = 4)	Metz (power = 12)	No filter
Butterworth (ν_c = 0.15)	0.66	0.1	0.001
Metz (power = 4)	—	0.06	0.002
Metz (power = 12)	—	—	0.003

filter functions can aid in selecting the proper operating point for a given filter function. This study suggests that the Metz filter at power 12 should not be used if one prefers to operate with a conservative decision criterion.

power 12. The two-tailed p values of these tests are shown in Table 2. When the paired t-test was then used to test differences in TPF at FPF values of 0.05, 0.1, 0.2, 0.3, 0.5, 0.7, and 0.9, there was no significant difference between the Butterworth and Metz 4 at any FPF. The Metz 12, however, was significantly worse than both the Butterworth and Metz 4 in terms of TPF at FPF values of 0.05, 0.1, and 0.2. Table 3 shows the two-tailed p values of these tests.

The results of this ROC study, then, agree well with the 2AFC finding that smoothing, in general, improves detectability in these images. And like the 2AFC experiment, the ROC study did not demonstrate any difference in observer performance with the Butterworth filtered images at ν_c = 0.15 cycles/pixel and Metz filtered images at a power of 4. The results of the two observers studies, however, did disagree in a couple of ways. First, the area under the curve, A_z, in the ROC study was depressed relative to the 2AFC score. This may be due to variance in performance across observers since the two studies did not use exactly the same observers. Second, in the ROC study but not in the 2AFC study, the Metz at power 12 performed significantly worse than the Butterworth filter at 0.15 cycles/pixel and Metz filter at power 4. This descrepancy could also be the result of variance in performance between observers of the two studies.

An interesting finding from the ROC study was that the Metz filter at power 12 scored worse than the other two filters only at low FPF values. Apparently, observers cannot perform well with this filter when forced to be conservative in their diagnostic calls. If the observer is allowed to be liberal in his calls, he performs as well with the Metz at power 12 as with Metz at power 4 and the 0.15 cutoff frequency Butterworth filter. Information concerning the shape of the ROC curves of these

REFERENCES

1. Gullberg GT. True three-dimensional reconstruction in single photon emission computed tomography. *J Nucl Med* 1983; 24:81.
2. King MA, Doherty PW, Schwinger RB, Jacobs DA, Kidder RE, Miller TR. Fast count-dependent digital filtering of nuclear medicine images: concise communication. *J Nucl Med* 1983; 24:1039–1045.
3. King MA, Schwinger RB, Doherty PW, Penney BC. Two-dimensional filtering of SPECT images using the Metz and Wiener filters. *J Nucl Med* 1984; 25:1234–1240.
4. King MA, Schwinger RB, Penney BC. Variation of the count-dependent Metz filter with imaging system modulation transfer function. *Med Phys* 1986; 13:139–149.
5. Beck RN, Schuh MW, Cohn TD, Lembares N. Effects of scattered radiation on scintillation detector response. In: *Medicine radioisotope scintigraphy, Vol. 1.* Vienna, IAEA, 1969: 595–616.
6. Atkins FB. Monte Carlo analysis of photon scattering in radionuclide imaging. PhD Thesis, The University of Chicago, Chicago, IL, 1978.
7. Beck RN, Rossmann K. Some fundamental concepts in radioisotope imaging. 12th International Congress of Radiology, Tokyo. Book of Abstracts, 1969:146.
8. Ehrhardt JC, Oberley LW, Lensink SC. Effect of a scattering medium on gamma-ray imaging. *J Nucl Med* 1974; 15:943–948.
9. Green DM, Swets JA. Signal detection theory and psychophysics. Huntington, NY: Robert E. Krieger Publishing Co., 1974.
10. Metz CE. ROC methodology in radiologic imaging. *Radiology* 1986; 21:720.
11. Swets JA, Pickett RM. Evaluation of diagnostic systems: methods from signal detection theory. New York: Academic Press, 1982.
12. Metz CE, Wang P, Kronman HB. A new approach for testing the significance of differences between ROC curves measured from correlated data. In: Deconinck F, ed. *Information processing in medical imaging.* The Hague, Martinus Nijhoff, 1984: 432–445.

TABLE 3
Two-Tailed p Values from Paired t-Tests of the Difference in TPF at a Given FPF

	Metz (power = 4)							Metz (power = 12)						
FPF=	0.05	0.1	0.2	0.3	0.5	0.7	0.9	0.05	0.1	0.2	0.3	0.5	0.7	0.9
Butterworth (ν_c = 0.15)	1.0	0.95	0.70	0.54	0.50	0.64	1.0	0.10	0.05	0.08	0.24	0.48	0.60	0.58
Metz (power = 4)	—	—	—	—	—	—	—	0.18	0.20	0.20	0.28	0.66	0.76	0.60